Published in final edited form as:
Curr Biol. 2021 September 13; 31(17): 3820–3833.e4. doi:10.1016/j.cub.2021.06.053.

Spinal V1 neurons inhibit motor targets locally and sensory targets distally

Mohini Sengupta[1], **Vamsi Daliparthi**[1], **Yann Roussel**[2,3], **Tuan Vu Bui**[2], **Martha W. Bagnall**[1]

[1]Washington University School of Medicine, Department of Neuroscience, St Louis, MO, USA.

[2]Brain and Mind Research Institute, Centre for Neural Dynamics, Department of Biology, University of Ottawa, Ottawa, Canada.

[3]Blue Brain Project, École Polytechnique Fédérale de Lausanne, Geneve, Switzerland.

Summary

Rostro-caudal coordination of spinal motor output is essential for locomotion. Most spinal interneurons project axons longitudinally to govern locomotor output, yet their connectivity along this axis remains unclear. In this study, we use larval zebrafish to map synaptic outputs of a major inhibitory population, V1 (Eng1+) neurons, which are implicated in dual sensory and motor functions. We find that V1 neurons exhibit long axons extending rostrally and exclusively ipsilaterally for an average of 6 spinal segments; however, they do not connect uniformly with their post-synaptic targets along the entire length of their axon. Locally, V1 neurons inhibit motor neurons (both fast and slow) and other premotor targets including V2a, V2b and commissural pre-motor neurons. In contrast, V1 neurons make robust long-range inhibitory contacts onto a dorsal horn sensory population, the Commissural Primary Ascending neurons (CoPAs). In a computational model of the ipsilateral spinal network, we show that this pattern of short range V1 inhibition to motor and premotor neurons underlies burst termination, which is critical for coordinated rostro-caudal propagation of the locomotor wave. We conclude that spinal network architecture in the longitudinal axis can vary dramatically, with differentially targeted local and distal connections, yielding important consequences for function.

Graphical Abstract

Corresponding Author and Lead contact: Martha W. Bagnall, bagnall@wustl.edu, Twitter: @MarthaBagnall.

Author contributions:
M.S. and M.W.B. conceived the project. M.S. performed the electrophysiology and confocal imaging experiments and analyzed the data. V.D., M.W.B., Y.R. and T.V.B built the computational model. V.D. and M.W.B. generated data from the model. M.S. and M.W.B. wrote the manuscript with input from all other authors.

Declaration of interests:
The authors declare no competing interests.

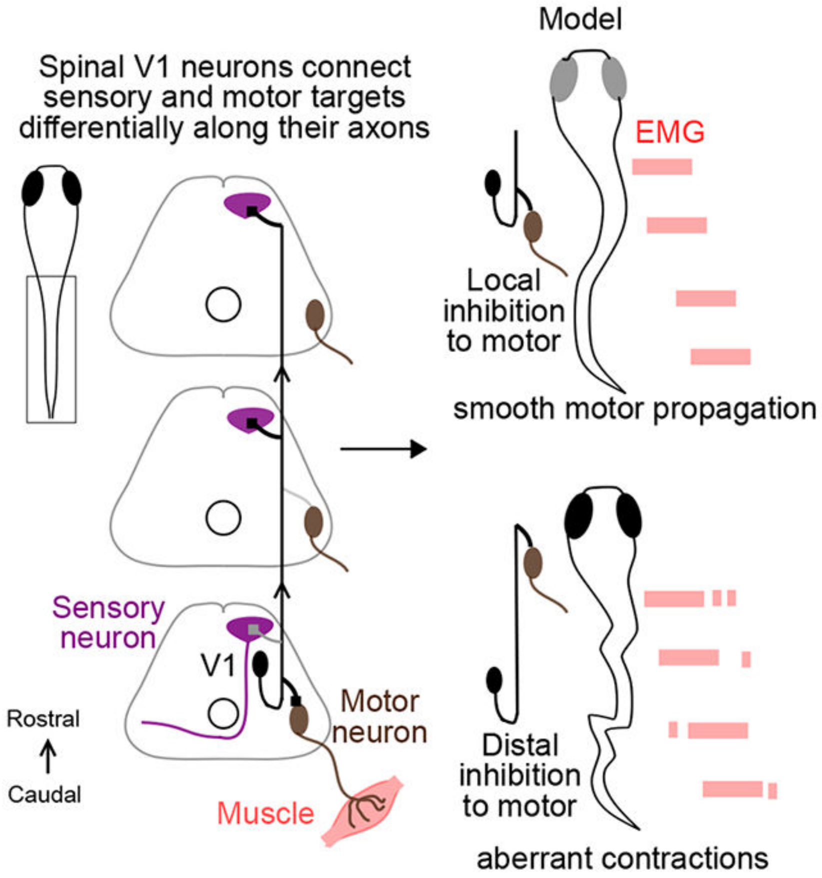

eTOC Blurb

The structure of neuronal connectivity is key to function. In this study, Sengupta et al. show that spinal V1 neurons exhibit differential connectivity to their sensory and motor post synaptic targets in the longitudinal axis and that this pattern of inhibition is critical for locomotor behavior.

Introduction

Neuronal connectivity is key to function. In cortex, the structure of inhibitory circuits influences synaptic gain, spike timing, and membrane potential oscillations [1]. In vertebrates, the spinal cord contains local circuits necessary and sufficient for producing movement. The spinal cord houses motor neurons and a range of distinct interneuron classes, the interplay of which results in a rich repertoire of movements [2]. Despite the importance of spinal interneurons in producing these movements [3-6], their circuit architecture remains largely unclear [7-13].

The spinal cord is elongated in the longitudinal or rostro-caudal (R-C) axis, which consists of many repeated segments. Coordination along this axis is crucial for locomotion [14,15], yet organization of neurons in this dimension is poorly understood. Interestingly, blockade of glycinergic neurons disrupts R-C coordination independently of left-right alternation, implying that ipsilateral inhibition is vital for locomotor propagation [16].

Most spinal interneurons, including ipsilateral inhibitory neurons, project axons spanning several segments along the R-C axis [17-21]. Here, taking advantage of the transparency and accessibility of the intact spinal cord in larval zebrafish, as well as its significant homology with other vertebrates, we mapped connectivity along the R-C axis in a major ipsilateral inhibitory population: V1 neurons.

V1 interneurons are marked by the expression of Engrailed1 (Eng1) transcription factor across vertebrates [19,22,23]. Genetic ablation of these neurons reduces locomotor speeds in both zebrafish [4] and mice [6,24] indicating that speed regulation is a primitive function of these neurons. V1 neurons have also been implicated in flexor-extensor alternation [25,26] and connectivity studies have suggested these neurons additionally gate sensory signals during locomotion [19,23]. It is unknown whether and how the motor and sensory functions of V1 neurons are organized along the longitudinal axis of the spinal cord.

Using a combination of single cell labelling, optogenetics and electrophysiology in vivo, we mapped synaptic connectivity from V1 neurons to eight motor and sensory spinal populations. Our results reveal that V1 neurons exhibit differential connectivity as they traverse the spinal cord longitudinally. Despite projecting long axons spanning > 5 segments, V1 neurons inhibit motor targets only locally, but inhibit sensory targets over a long range. Using our connectivity map as the basis of a simplified model of the ipsilateral spinal cord, we show that this structure of V1 inhibition is critical for maintaining smooth propagation of locomotion.

Results

V1 neurons project primarily ascending axons spanning 5-10 spinal segments

V1 neurons are distributed along the length of the spinal cord[19,27], but there are no systematic analyses of their cell numbers and morphology in zebrafish. Using confocal imaging of the *Tg(eng1b:Gal4,UAS:GFP)* fish line, we obtained cell counts of GFP+ neurons all along the length of the zebrafish larval spinal cord, which is partitioned by myotomes into ~28 segments. V1 neurons were uniformly distributed along the rostro-caudal (R-C) axis, with an average of 18.9 ± 5.6 V1 neurons per segment (Fig. 1A, B; mean ± SD, N=10 larvae). Next, to optimize design of our subsequent mapping experiments, we investigated the extent of V1 axonal projections in the R-C axis., V1 neurons project axons ipsilaterally and rostrally[19,22,23] with a subset also exhibiting descending axonal branches[19,28,29]. To study morphology, we performed single cell labelling in the *Tg*(*eng1b:Gal4,UAS:RFP)* fish line using two approaches: single cell electroporation of fluorescently tagged dextran or micro-injection of a *UAS:Dendra* plasmid construct, followed by confocal imaging of single cells. Both techniques yielded similar results and were pooled for analysis. Fig. 1C shows an example of a representative V1 neuron labeled with *UAS:Dendra*. All V1 neurons (N=28 cells from 18 larvae) displayed an exclusively ipsilateral ascending axon, extending for a median of 6 segments. 17 / 28 neurons (60.7%) also exhibited a short descending axon branch spanning a median of 1 segment (Fig. 1D).

Previous studies in zebrafish have reported V1 neurons with longer descending axons (up to 8 segments)[19]. Therefore, in a separate set of experiments, we injected a BAC construct, *eng1b:GFP*, replicating previous studies[19]. These injections yielded V1 neurons with pure ascending axons (1/5), neurons with ascending axons and short descending branches (2/5), and neurons with ascending axons and long descending branches (2/5) (Fig. S1A). To check if all the BAC labeled cells were represented in the *Tg(eng1b:Gal4)* line, we injected the BAC construct in this background. 3/5 neurons co-expressed both *eng1b* labels (Fig. S1b top and middle) but overlap was weak or non-existent in the remaining 2 neurons (Fig. S1b, bottom). In addition, the BAC yielded label in many non-V1 neurons, such as cerebrospinal fluid contacting neurons (CSF-cNs), Commissural Bifurcating neurons (CoBLs) and sensory Dorsal Longitudinal Ascending neurons (DoLAs). Therefore, the BAC construct appears to preferentially label a rarer subset of V1 neurons with long descending axons. D-V positions of V1 somata were similar across all axon morphologies (Fig S1c). Based on these results, we concluded that irrespective of their descending axon morphology, all V1 neurons exhibited long ascending axons. We therefore chose to build a connectivity map covering 7 segments in the ascending direction and 2 segments in the descending to encompass the rostral axonal extent of all V1 neurons, and a significant subset of the caudal extent.

Patterned optical stimulus evokes localized and reliable spiking in V1 neurons

To create a map of V1 connectivity via optical stimulation, we generated a transgenic fish line, *Tg(eng1b:Gal4,UAS CatCh)*, in which the calcium permeable channelrhodopsin CatCh[30] was expressed in V1 neurons (schematic, Fig. 2A). V1 cell counts in this line matched our results from *Tg(eng1b:Gal4,UAS:GFP)* fish line (Fig. S2A, B) confirming widespread expression of CatCh. We first calibrated the optogenetic stimulation to ensure it was only effective at eliciting spiking when light was targeted near the soma of a V1 neuron, not its axon. We recorded whole cell from V1 neurons while projecting 20 x 20 µm squares of blue light via a digital micromirror device (DMD). A 4x4 grid of these squares was delivered in sequence and effectively tiled each spinal segment (Fig. 2B). V1 neurons were recorded in current clamp mode and held at their resting membrane potential which was −76.5 ± 5.6 mV (average ± SD, N=17 neurons). Membrane potential responses of an example V1 neuron is shown in Fig. 2C (left). Most squares elicited only subthreshold responses (black), but illumination of the square directly on the soma (black dot) or in a few surrounding squares effectively drove spiking (red traces). Spiking elicited by illumination is represented as a heat map of spike count (Fig. 2C, right). This spatially restricted response was observed for all 17 V1 neurons recorded (Fig. S2C).

Next, because our primary objective was to map connectivity in the R-C axis, we tested the efficacy of the optical stimulus by translating it longitudinally. An identical 4x4 illumination pattern was projected first one and then two segments away from the recorded cell, in the rostral and caudal directions. As shown in the representative example, illumination outside of Segment 0 (the recorded segment containing the V1 soma) rarely elicited any appreciable spiking responses (Fig. 2D, E). Antidromically evoked spiking was recorded in only 2 out of 17 cells, and the number of spikes elicited was low. Repeated presentation of on-soma illumination reliably evoked spiking in 7 out of 10 neurons (Fig. 2F). Taken together, these data indicate that this optical stimulation is able to evoke V1 spiking only within the illuminated segment, allowing us to use this method for subsequent longitudinal mapping of connectivity.

Spinal neurons are known to be topographically arranged and recruited for different speeds of locomotion[31]. These speed modules often also exhibit different passive and active properties[32,33]. We therefore analyzed the latency of the first spike and total elicited spike counts with respect to V1soma positions. As shown in Fig. S2D and E, V1 neurons exhibited a broad distribution of spike latencies and spike counts which did not show any apparent relationship to soma D-V position. Therefore, the optical stimulus is equally effective across the D-V axis of the spinal cord.

V1 neurons inhibit motor neurons locally

Anatomical and physiological studies indicate that V1 neurons directly inhibit motor neurons in mice[26,28,29,34], zebrafish[4,19], and tadpoles[23]. Based on the long ascending projections of V1 axons, we anticipated that this inhibition would extend over ~6 segments rostrally from each V1 neuron. To examine the spatial extent of V1 inhibition, we recorded from fast primary and slow secondary motor neurons while delivering optical stimulation as above in *Tg(eng1b:Gal4, UAS:CatCh)* larvae. Primary MNs (pMNs) are identifiable by their large, laterally placed somata, low input resistances, and extensive axon arborization in characteristic patterns[32] and were validated by post-hoc cell fills. In this and subsequent experiments, neurons were held at 0 mV in voltage clamp with a cesium-based internal solution and glutamate receptor blockers in the bath to isolate IPSCs. The patterned optical stimulus was delivered one segment at a time, caudally up to 7 segments and rostrally up to 2 segments relative to the recording site, while recording light evoked IPSCs (schematic, Fig. 3A). Fig. 3B shows representative traces of evoked IPSCs in pMNs (top) when the optical stimulus was presented 1, 3 and 7 segments caudal to the recording site, respectively. pMNs received robust IPSCs when V1s were stimulated 1 segment caudally, but surprisingly, this inhibition diminished drastically as the optical stimulation was translated further caudally (Fig. 3B, top). Charge transfer of the evoked IPSCs (Fig. 3C, inset) (see Methods and Fig. S3) for segments 0, 1, and 2 was significantly different from noise (Fig. 3B, bottom; N=26 neurons; Wilcoxon Sign Rank Test, $p < 0.01$). In contrast, the responses for segments 3, 5, and 7 were indistinguishable from noise. Charge transfer elicited by the descending axons, in Segments −1 and −2, was small in amplitude and significantly different from noise only for Segment −1. These results indicate that V1 neurons only provide appreciable inhibition onto pMNs located close to the V1 soma.

To test whether these inputs were monosynaptic in nature, we selected one square in the 4x4 grid and illuminated it with a 20 Hz train of five 20 ms pulses[35]. pMNs received reliable V1 input during this high frequency stimulation at Segments 0 and 1 but not Segment 5 (Fig. S4A). For all cells (5/5), IPSCs were evoked at a consistent latency with low jitter (Fig. S4B). These IPSCs were abolished by strychnine and TTX (Fig. S4D, E), consistent with a monosynaptic, glycinergic connection.

To test V1 connectivity to slow, secondary motor neurons (sMNs), we crossed the *Tg(eng1b:Gal4,UAS:Catch)* line to a motor neuron reporter line, *Tg*(*mnx:pTagRFP*)[32]. Recordings targeted smaller motor neurons, and optical stimulation was performed as above. sMNs also showed evoked IPSCs for V1 stimulation locally (Segments 0-3) but not long-range (Segments 5,7) (Fig. 3C, N=11 neurons; Wilcoxon Sign Rank Test, $p < 0.01$). Thus, similar to pMNs, sMNs are inhibited predominantly by local V1 neurons.

This decrease in evoked inhibition onto neurons located distally from the segment of stimulation could arise from a) a decrease in the *number* of V1 neurons connecting to motor neurons at longer distances, or b) a decrease in the *strength* of individual connections for long-range, as opposed to local, synapses from V1 neurons onto motor neurons. To differentiate between these two possibilities, we first analyzed the number of grid squares that evoked IPSCs in each segment. Because V1 neurons are evenly distributed along the R-C axis (Fig. 1A, B) and our patterned stimulus uniformly covered one full segment, the number of squares evoking IPSCs can be used as a proxy for the number of connections. Fig. 3D shows a significant decrease in the percent of squares eliciting IPSCs along the R-C axis for both pMNs and sMNs (Kruskal Wallis Test and post hoc Tukey's test, $p < 0.01$), suggesting that fewer V1 neurons in the distal segments contact motor neurons. As a measurement of the strength of individual synaptic connections, we analyzed the peak amplitudes of the evoked IPSCs (Fig. 3E). There was no significant difference between segments (Kruskal Wallis Test, $p > 0.01$), suggesting that the strength of individual connections is consistent along the R-C axis. Overall, these data indicate that despite projecting axons 5-10 segments rostrally, V1 neurons only inhibit local primary and secondary motor neurons (< 3 segments), and that this bias in connectivity is set by the number of V1 neurons synapsing on each target, not by a change in synaptic weights.

V2a and V2b neurons also receive inhibition locally from V1 neurons

To determine whether this pattern in V1 connectivity extends to other potential synaptic targets, we next examined their inputs onto V2a and V2b cells, which arise from a final division of the p2 progenitor class[36]. V2a (*vsx2*+, previously known as *chx10* or *alx*) neurons are premotor[8,20,37], glutamatergic, excitatory drivers of locomotion[38-40], and are important V1 targets for speed control[4]. V2b (GATA3+) neurons, on the other hand, are also premotor but glycinergic/GABAergic, and their activation slows down locomotion[41]. We investigated the structure of V1 connectivity to these two premotor classes by crossing the *Tg(eng1b:Gal4,UAS:CatCh)* line to either *Tg(vsx2:lox-Dsred-lox:GFP)*[42] or *Tg(gata3:lox-Dsred-lox:GFP)*[41] to target recordings to V2a and V2b neurons, respectively (schematic, Fig. 4A). As shown in Fig. 4B, C, both V2a and V2b neurons could be robustly inhibited by optical stimulation of V1 neurons up to 3 segments away from the recording site but not at longer distances. Charge transfer values for V2a neurons was significantly different from noise at segment 0-5 (N=14 neurons; Wilcoxon Sign Rank Test, $p < 0.01$) but the effect was even more local for V2b neurons showing significant inhibition only up to 3 segments away (Fig. 4C, bottom; N=8 neurons; Wilcoxon Sign Rank Test, $p < 0.01$). V2a, but not V2b neurons also showed significant responses when V1 neurons were stimulated rostral to the recording site (Fig. 4B, Segment −2). As with motor neurons, the number of squares capable of evoking IPSCs decreased steadily as the optical stimulus was translated caudally, indicating fewer V1 neurons connecting with V2as/V2bs distally (Fig. 4D; Kruskal Wallis Test, $p < 0.01$). An analysis of the conductances of IPSCs in different segments did not show any longitudinal bias for either V2a or V2b neurons (Fig. 4E; Kruskal Wallis Test, $p > 0.01$) indicating that the differences in the connectivity along the R-C axis are shaped by a difference in the number of distally contacting V1 neurons and not by a change in the strength of the connections.

CoPA neurons receive both local and distal V1 inhibition

In addition to their role in motor control, V1 neurons and their counterparts in Xenopus (aINs) are known to govern sensory gating[23] and project to the dorsal horn[19,23,27]. In larval zebrafish, V1 neurons have been shown to directly contact Commissural Primary Ascending (CoPA) neurons[19], a glutamatergic dorsal horn sensory population which are recruited in response to touch and cause contraversive flexion[43,44]. Recent studies have identified a potential genetic marker for CoPA neurons, Mafba[45], which suggests that, these neurons are likely homologous to deep dorsal horn Laminae III/IV glutamatergic neurons, arising from the dI5/dIL$_B$ precursor populations that receive afferent inputs carrying innocuous mechanoreceptive signals[46,47]. During early spontaneous coiling and later in burst swimming, the CoPAs receive glycinergic inhibition that gates their activity[43], a potential source being V1 neurons. Therefore, we next examined the longitudinal structure of V1 connectivity to CoPA neurons. CoPAs are readily distinguished by their dorsal location, large triangular somas and elongated dendrites extending several segments[44,48], and were identified post hoc with cell fills. As above, we recorded IPSCs from CoPA neurons while delivering V1 optical stimulation along the R-C axis (Fig. 5A). Surprisingly, in contrast to our observations in motor targets, CoPA neurons received robust V1-mediated inhibition from stimulation both locally and long-range, even up to 9 segments away (Fig. 5B). Charge transfer values for all segments from 0-9 were significantly different from noise (Fig. 5B, N=12 neurons; Wilcoxon Sign Rank Test, $p < 0.01$). No appreciable V1 connectivity was observed from the descending axonal branch of V1 neurons to the CoPAs.

We considered the possibility that as V1 axons ascend and travel dorsally, they connect indiscriminately to dorsal horn (sensory) targets. Therefore, we targeted another dorsal horn sensory population, the Dorsal Longitudinal Ascending (DoLA) neurons, a GABAergic population expressing Tbx16 and Islet1[49] that is likely homologous to GABAergic Islet$^+$ / dI4 cells in Lamina I-III of mouse spinal cord[50]. However, V1 neuron stimulation evoked no synaptic inputs to DoLAs, either locally or distally (Fig. 5C; N=5 cells).Therefore, the V1 connectivity to CoPAs reflects specific targeting within the dorsal horn. An analysis of the number of squares in the grid that evoke IPSCs in CoPAs and IPSC conductances revealed that there was no significant difference between local (Segments 0-1) and distal segments (5-7) (Fig. 5D,E; Kruskal Wallis Test, $p > 0.01$) indicating that a similar number of V1 neurons connect to CoPAs both locally and distally the strength of V1 connectivity is maintained.

Other pre-motor neurons receive only local inhibition from V1 neurons

Collectively, these data indicate that V1 neurons exhibit a bias in their local vs. distal connectivity. What dictates this bias? One hypothesis is that V1 neurons connect locally to all ipsilaterally projecting targets (MNs, V2as and V2bs) but connect more broadly to contralaterally projecting targets (CoPAs). Alternatively, this bias could be based on motor related (MNs, V2as and V2bs) versus sensory (CoPAs) identities. To test these hypotheses we targeted ventral horn commissurally projecting neurons that are likely dI6/V0 identity.

These neurons comprise both inhibitory and excitatory[51-53] subsets but are characterized by a common morphological motif: a dorsal soma and a commissural, bifurcating axonal trajectory[51,52]. We identified these neurons post hoc with cell fills and categorized them as Commissural Pre-motor (CoPr). V1 optical stimulation was performed as before (Fig. 6A). Interestingly, CoPr neurons also received only local inhibition from V1 neurons (Fig. 6B, C). We also analyzed the number of squares evoking IPSCs per segment and conductances of IPSCs. No significant differences between segments were observed for either of these parameters (Fig. 6C, D). Thus, these data support the notion that V1 neurons connect locally to motor-related targets and long-range to sensory targets.

To test the specificity of V1 connectivity to motor targets, we also recorded from other V1 neurons, putative Commissural Secondary Ascending (CoSA) neurons (corresponding to the $V0_V$ population)[54] and one Commissural Local (CoLo) interneuron (corresponding to dI6)[55]. Of these targets, only V1 neurons themselves received any appreciable V1-mediated inhibition (Fig. S5), showing that this V1 connectivity map is indeed highly specific.

Fig. 6F summarizes connectivity data to all the targets tested. The magnitude of charge transfer is not directly comparable across neurons, because inhibition's effects will depend on its strength relative to the total conductance of the target neuron. Therefore, we normalized the charge transfer for each neuron to that cell's intrinsic conductance (i.e., the inverse of input resistance) (Fig. 6F, bottom). We clearly observe differential connectivity from V1 neurons to sensory (CoPA) as compared to motor related (pMN, sMN, V2a, V2b and CoPr) post synaptic targets. This result is also visible in a charge transfer plot for every neuron shown individually (Fig. S6A-F). Because sensory and motor related targets are found in the dorsal and ventral horns, respectively[2], this heat map of V1 connectivity along the R-C axis also showed a dorsal – ventral structure. Taken together, these data show that although V1 neurons extend long, ascending axons spanning several spinal segments, they do not uniformly connect to all post synaptic targets along the extent of their axons. Closer to their somata (locally), V1 neurons preferentially inhibit motor and pre-motor targets. In contrast, as the axon travels rostrally, connectivity with motor and pre-motor neurons falls off sharply, and instead it inhibits sensory CoPAs (schematized in Fig. 6F, top).

V1 connectivity to local motor populations is required for longitudinal coordination

To evaluate the importance of the structure of ipsilateral inhibition on zebrafish swimming behavior, we developed a computational model of the zebrafish spinal cord. Since V1 neurons do not have any effect on left-right alternation[6,26], we modeled only the unilateral cord. V2b neurons and CoPAs were excluded; V2b downstream targets are unknown, and CoPAs are thought to respond to unexpected touch, not during normal locomotion[43]. This reduced model comprised a cluster of pacemaker neurons and a 15 hemisegment spinal cord, consisting of MNs, V2a, and V1 neurons (Fig. 7A, see Methods for detailed description) and was adapted from a larger model[56]. Individual neurons were simulated with ordinary differential equations as described in the Izhikevich model[57]. V2a neurons formed glutamatergic synapses onto other V2as, V1s, and MNs, while V1s formed glycinergic synapses onto V2a and MNs. The spiking activity of MNs served as the readout of our spinal cord model.

We first simulated a network that matched our experimental results, with local V1 inhibition (within 1 to 3 segments) onto V2as and MNs (schematic, Fig. 7B; connectivity grid, 7C, left). This model recapitulated swim beats with clean rostro-caudal propagation of a locomotor wave (Fig. 7D, left). The tail beat occurred at a frequency of 21.2 Hz (47.08 ± 1.18 ms). Next, we tested the consequences of changing V1 inhibition from local to distal by shifting V1 connections onto MNs and V2as located 4-6 segments rostrally (Fig. 7B, C, middle; asterisks denote the changed connections). The total amount of inhibition was held constant compared to the first model; only the relative position of the connections was altered. This reduced tail beat frequency (19.0 Hz, 52.57 ms ± 0.64 ISI, Kruskal Wallis Test and post hoc Tukey Kramer, $p<0.01$) and also produced extraneous spikes in MNs outside of swim beats, thus reating erratic oscillations and aberrant “contractions” that disrupted the smooth rostro-caudal propagation (Fig. 7D, middle). To quantify these effects, we analyzed the time of spiking in motor neurons across a normalized cycle. The long-range connectivity model exhibited an extra burst of MN spiking following the tail beat compared to the local connectivity model (Fig. 7E, left). To determine whether normal network function is impacted more by long-range V1 to V2a connectivity or long-range V1 to MN connectivity, we simulated a hybrid network with local V1 to V2a but long-range V1 to MN connections (Fig. 7B, C, right). This network exhibited a similar frequency of swim beats (21.8 Hz, 45.9 ms ± 1.04, Kruskal Wallis Test and post hoc Tukey Kramer) as our experimentally derived model but still produced extraneous spikes following the tail beat (Fig. 7E, right). We also simulated the reverse hybrid model with long-range V1 to V2a but local V1 to MN connections; this network had fewer extraneous spikes but exhibited slower swim beats compared to all local V1 inhibition (17.8 Hz, 56.13 ± 0.43 ms vs, Kruskal Wallis Test and post hoc Tukey Kramer, $p<0.01$) (Fig. S7). Taken together, these simulations show that local V1 connectivity is crucial for normal spinal cord rhythmicity, and that alterations in this network structure affect both swim frequency and network reliability.

Discussion

In this study, we show that V1 neurons exhibit differential connectivity to targets located proximally vs distally along the longitudinal axis of the spinal cord. Specifically, V1 neurons inhibit motor and premotor targets locally, and sensory targets further away, a unique connectivity pattern not described before. Furthermore, we show that this configuration has critical functional implications for motor burst termination and locomotor frequency. The results demonstrate that circuit architecture can vary along the longitudinal axis of the spinal cord and is important to circuit function.

Heterogeneity of V1 neurons

Recent work in mice has shown that V1 neurons can be divided into 50 transcriptionally different subtypes that exhibit distinct physiology and position in the ventral horn, implying different functions[58]. Our anatomical experiments revealed different morphologies of V1 neurons, hence we (Fig. 1C, D and Fig. S1A), considered the alternate hypothesis that differential connectivity to motor and sensory targets is accomplished by two different V1 subclasses: i.e., ascending V1s project long distances and connect only to sensory CoPAs whereas bifurcating V1s only project locally and connect to motor targets. However, our data do not support this hypothesis: there are no differences in the ascending axon trajectories (axonal length and D-V positions of the axons) or the D-V position of the somata between these subtypes (Fig. S1C). Therefore, we conclude that individual V1 neurons likely connect to both sensory and motor targets differentially along their projections.

In limbed vertebrates, multiple functional subclasses of V1 neurons have been identified: Renshaw cells involved in feedback control, and Ia inhibitory neurons participating in flexor-extensor reciprocal inhibition[59]. Both these subclasses contact motor neurons but receive different inputs[60]. Since our data maps the output of V1 neurons, and not the input, we cannot evaluate whether V1 neurons in our study are like Renshaw cells or Ia inhibitory neurons. Future delineation of subtypes of V1 neurons in zebrafish, including analysis of their inputs from motor neuron collaterals[61], will help elucidate conserved functions of these neurons in motor control.

V1 influence on speed regulation and motor coordination.

Ablating or inhibiting V1 neurons results in slower speeds of locomotion in both mouse and zebrafish[4,6,24]. V1 neurons appear to govern speed through two different mechanisms: burst termination in fast motor neurons and suppression of spiking in slow motor neurons[4]. Previous studies have reported that in phase inhibition affecting motor neuron spike after hyperpolarization is important for rostro-caudal propagation[62]. Consistent with this we show that local V1 input to motor neurons was required to successfully terminate motor bursts in our spinal cord model, allowing smooth propagation of the locomotor wave (Figure 7). Like motor neurons, V1 neurons can be categorized into fast and slow subtypes based on the speed at which they are recruited[4]. Both fast and slow V1 neurons inhibit slow motor neurons albeit at different swim frequencies[4]. In line with this, we also observed that the extent and impact of V1 inhibition was greater in slow sMNs after normalization to conductance (Fig. 6F).

Our results also confirm that V1 neurons directly inhibit V2a neurons[4]. Moreover, results from our model indicate that local connectivity to V2as is necessary to maintain fast speeds of locomotion (Fig. 7 and Fig. S7). V2a neurons are also arranged in speed modules [31]. To test whether fast and slow V2a neurons show different V1 connectivity, we analyzed the charge transfer of IPSCs recorded in V2a neurons with respect to their D-V positions but did not find any significant trends (data not shown) implying that V1 connectivity to V2a is local irrespective of their speed modules. Finally, within speed modules, V2a neurons are also known to have different morphologies (descending and bifurcating) that exhibit different input resistances and other passive and active properties[8,37]. We also analyzed the charge transfer of V2a neurons with respect to their input resistances but did not find any significant trends (data not shown).

V1 neurons recruited during fast movements are thought to be located ventrally to slow V1 neurons[31]. We found no differences in spiking latencies or spike counts between dorsal and ventral V1 neurons (Fig. S2D, E). Additionally, we analyzed V1-evoked charge transfer based on the D-V position of the V1 optogenetic stimulus but did not find any clear relationships. However, because our optogenetic stimulus activated V1 neurons both under and adjacent to the light (Fig. S2C), these results are inconclusive.

Another spinal population affecting locomotor speed is the V2b class, an inhibitory, ipsilaterally projecting interneuron population. Loss of V2b neurons result in an increase in locomotor speed, suggesting that V2bs act as brakes on locomotion[41]. Direct inhibition of V2b neurons by V1 neurons, resulting in disinhibition of motor neurons, could be yet another mechanism by which V1 neurons facilitate high locomotor speeds. Future analysis with models including different speed modules and our local connectivity map will elucidate fine control of these various mechanisms for speed regulation.

V1 affects sensory neurons broadly

Our results show robust inhibition of sensory CoPA neurons by V1 neurons, in agreement with previous observations[19,23]. V1 neurons in mouse also project to the deep dorsal horn[27], but their specific targets and functions are not known. We predict that the mafba+ $dI5/dIL_B$ neurons are likely targets. Additionally, we show that V1 neurons connect with CoPAs extensively and long-range (up to 7-9 segments), suggesting that sensory gating by V1s is both spatially and temporally broad. Correspondingly, inhibition onto CoPA neurons is thought to function as a shunt, with less temporal precision[43]. Previous reports have shown that BAC labeled V1 neurons with both long ascending and descending projections inhibit CoPA neurons in both directions[19] in line with our proposed function of broad sensory gating. Since all our physiology was performed in *Tg(eng1b:Gal4)* lines that do not or weakly label this V1 population, we were not able to test the long descending connectivity to CoPA neurons.

Recent studies have pointed to an important role of CSF-cNs, another inhibitory, ipsilateral, and ascending spinal population (CSF-cNs), in regulating power of locomotion in response to spinal curvature[9,35,63,64]. In future, it will be extremely relevant to study how these ascending sensory pathways are integrated for effective motor control.

Other examples of differential connectivity

In this study we show that V1 axons target different post-synaptic populations as they traverse the length of the spinal cord. Other projection neurons also show differential connectivity along their axons, but only because they travel to multiple distinct regions of the nervous system (for example, corticospinal neurons projecting to both pons and spinal cord[65]). In contrast, cortical pyramidal neurons target similar postsynaptic partners regardless of whether they are synapsing locally or long-range[66]. The differential local to long-range connectivity within one region that we describe here appears unusual; however, it might be a common strategy in the spinal cord due to the propagation of locomotor activity that requires temporal patterning of spinal activity in the R-C axis.

Our results further demonstrate significant interconnectivity between spinal interneuron populations, an area that requires future characterization to help decipher the underlying neuronal code. Future studies aimed at exploring other dorsal horn targets and analysis of V1 subsets in zebrafish will help understanding the role of V1 neurons in encoding sensory-motor control.

STAR METHODS:

RESOURCE AVAILABILITY

Lead contact: Further information and requests for resources and reagents should be directed to and will be fulfilled by the lead contact, Martha Bagnall (bagnall@wustl.edu).

Materials availability: This study did not generate new unique reagents or transgenic lines.

Data and code availability: All data reported in this paper will be shared by the lead contact upon request.

Original code for the computational model used in this manuscript is available at https://github.com/bagnall-lab/V1_connectivity_project. DOIs are listed in the key resources table.

Any additional information required to reanalyze the data reported in this paper is available from the lead contact upon request.

EXPERIMENTAL MODEL AND SUBJECT DETAILS

All fish used for experiments were at larval stage from 4-6 days post fertilization (dpf) before the onset of sexual maturation. All experiments and procedures were approved by the Animal Studies Committee at Washington University and adhere to NIH guidelines.

Adult zebrafish (Danio rerio) were maintained at 28.5°C with a 14:10 light:dark cycle in the Washington University Zebrafish Facility up to one year following standard care procedures. Larval zebrafish (4–6 dpf) used for experiments were kept in petri dishes in system water or housed with system water flow. Animals older than 5 dpf were fed rotifers or dry powder daily.

Double transgenic animals that we refer to throughout this paper as *Tg(eng1b:Gal4,UAS:CatCh*) were created by crossing the transgenic line *Tg(eng1b-hs:Gal4)*[67] with a stable *Tg(UAS:CatCh)*[41] line. For targeting V2a and V2b neurons, the *Tg(vsx2:loxP-DsRed-loxP-GFP*)[42], and *Tg(gata3:lox-Dsred-lox:GFP)*[41] lines, respectively, were crossed to *Tg(eng1b:Gal4,UAS:CatCh)* to generate triple transgenics. We generated the *Tg(mnx:pTagRFP)* line by injecting a construct kindly shared by Dr. David McLean.

METHOD DETAILS

Stochastic single cell labelling by microinjections: *Tg(eng1b:Gal4)/WT* embryos (depending on the experiment) were injected with a *UAS:Dendra* plasmid[68] (a gift from Dr. David McLean) or *eng1b:GFP* BAC[19] construct (a gift from Dr. Higashijima) at the 1-2 cell stage. Final plasmid DNA concentration was 10-15 ng/μl. The embryos were transferred to system water, regularly cleaned, and allowed to develop. At 4 dpf, larvae were screened for sparse expression of Dendra/GFP in the spinal cord and selected for confocal imaging.

Single cell labelling by electroporation: *Tg(eng1b:Gal4,UAS:GFP)* animals (4–6 dpf) were anesthetized in 0.02% MS-222 and fixed to a sylgard lined petri dish with custom made tungsten pins. One muscle segment was carefully removed to expose the underlying spinal cord. A pipette electrode (10-12 MΩ) filled with 10% Alexa Fluor 647 anionic dextran in potassium-based patch internal solution (see Electrophysiology methods for details), was positioned to contact the soma of the target neuron. Dye was electroporated into the cell via one to three 500 ms, 100 Hz pulse trains (1 ms pulse width) at 2–5 V (A-M systems Isolated Pulse Stimulator Model 2100). Confocal imaging was performed after 30 mins for dye filling.

Confocal imaging: 4–6 dpf larvae were anesthetized in 0.02% MS-222 and embedded in low-melting point agarose (1.5%) in a 10 mm FluoroDish (WPI). Images were acquired on an Olympus FV1200 Confocal microscope equipped with high sensitivity GaAsP detectors (filter cubes FV12-MHBY and FV12-MHYR), and a XLUMPlanFl-20x W/0.95 NA water immersion objective. A transmitted light image was obtained along with laser scanning fluorescent images to identify spinal segments. Sequential scanning was used for multi-wavelength images.

Electrophysiology: Whole-cell patch-clamp recordings were performed in larvae at 4–6 dpf. Larvae were immobilized with 0.1% α-bungarotoxin and fixed to a Sylgard lined petri dish with custom-sharpened tungsten pins. One muscle segment overlaying the spinal cord was removed at the mid-body level (segments 9–13). The larva was then transferred to a microscope (Nikon Eclipse E600FN) equipped with epifluorescence and immersion objectives (60X, 1.0 NA). The bath solution consisted of (in mM): 134 NaCl, 2.9 KCl, 1.2 $MgCl_2$, 10 HEPES, 10 glucose, 2.1 $CaCl_2$. Osmolarity was adjusted to ~295 mOsm and pH to 7.5. To record IPSCs, (2*R*)-amino-5-phosphonovaleric acid (APV; 10 μM) and 2,3-dioxo-6-nitro-7-sulfamoyl-benzo[f]quinoxaline (NBQX; 10 μM) were also added to the bath. Patch pipettes (7–15 MΩ) were filled with either of the following two internal solutions. Current clamp (recordings of V1 spiking): (in mM): 125 K gluconate, 2 $MgCl_2$, 4 KCl, 10 HEPES, 10 EGTA, and 4 Na_2ATP. Voltage clamp (IPSCs) (in mM): 122 cesium methanesulfonate, 1 tetraethylammonium-Cl, 3 $MgCl_2$, 1 QX-314 Cl, 10 HEPES, 10 EGTA, and 4 Na_2ATP. For both solutions, pH was adjusted to 7.5 and osmolarity to 290 mOsm. Additionally, sulforhodamine 0.02% was included in the patch internal to visualize morphology of recorded cells post-hoc. Recordings were acquired using a Multiclamp 700B amplifier and Digidata 1550 (Molecular Devices). Signals were filtered at 2 kHz and digitized at 100 kHz. For IPSCs, cells were recorded at +0.3 mV (after correction for liquid junction potential of 14.7 mV). Reported measurements of membrane potential in current clamp have been corrected for liquid junction potential which was 15 mV. The following drugs were bath applied where noted: tetrodotoxin (TTX; 1 µm), strychnine (10 µM).

Optogenetic Stimulation: A Polygon 400 Digital Micromirror Device (Mightex) was used to deliver optical stimulation. The projected optical pattern consisted of a 4x4 grid of 16 squares. Each square in the grid approximately measured 20µm x 20µm and covered 0-6 cells depending on position. One full stimulus pattern consisted of an ordered sequence of turning ON and OFF each of the 16 squares sequentially. For each small square, illumination consisted of a 20 ms light pulse (470 nm) at 50% intensity (4.6-5.2 µW under 60X, 1.0 NA). The sequence was triggered using a TTL pulse from the Digidata to synchronize the stimulation with electrophysiology. The objective was carefully positioned over a single spinal segment prior to stimulus delivery; for each new segment, the stage was manually translated and repositioned. V1 spiking reliability was measured by delivering multiple trials to a selected square that had evoked spiking on the first trial. A similar protocol was used for all segments to obtain reliable IPSCs for measurement of conductances. For the high frequency stimulation in Fig. S4, a single square was illuminated with a 20 Hz train of five 20 ms pulses.

Computational modeling: Zebrafish spinal cord networks were modeled in Python as a 15-segment ipsilateral network adapted from a larger model[56]. Pacemakers were located rostrally to the first segment. The Izhikevich neuron model was used to simulate individual cells in the network[57]. In these models, the subthreshold and suprathreshold dynamics of the membrane potential are described by several general differential equations[57]. Different firing behaviours can be generated by setting the following parameters for each neuron: *a:* recovery rate; *b:* sensitivity to spiking, *c*: reset voltage, *d*: after-spike reset rate and peak V: maximum voltage of a spike. We chose values of these parameters to reproduce firing behaviors observed in spinal neurons of larval zebrafish[4,8,32]. The reduced network modeled in this study included a cluster of rostrally located pacemaker neurons, V1 neurons, V2a neurons, and motor neurons (MNs). Each segment in the model incorporated a V2a neuron and a MN, with a single V1 neuron in every segment after segment 3. The network was driven using 5 electrically coupled pacemaker neurons (see Table S1 for Izhikevich parameters) and a linear descending gradient of tonic drive to V2a neurons. Pacemakers were electrically coupled to the 6 most rostrally located V2a neurons. MNs received glutamatergic drive from V2as and glycinergic drive from V1 neurons. Electrical synapses are modeled as ideal resistors following Ohm's law. Chemical synapses are modeled as a biexponential that accounts for rise and decay rates, as well as glycinergic and glutamatergic reversal potentials (see Table S2 for chemical synapse parameters). V2a neurons provided descending glutamatergic projections to other V2as and V1s located up to 3 segments away. V2a neurons also made bifurcating glutamatergic projections to motor neurons, connecting to caudal motor neurons up to 3 segments away, and rostral motor neurons up to 2 segments away. V1s formed glycinergic synapses with V2as and MNs; the structure of V1 projections onto V2as and MNs was manipulated to target either local (soma within 1 to 3 segments) or distal (soma located 4 to 6 segments away). Individual weights of glycinergic synapses formed by V1s were randomized from simulation to simulation using a gaussian distribution [0.5 ± 0.25 std]; the sum of the weights of all V1 to V2a and V1 to MN was maintained between simulations. Finally, physical length and speed of transmission between neurons was calibrated such that the rostro caudal delay of transmission between segments was around 1.6 ms, in line with experimental data[69]. Each network configuration was simulated 15 times to generate summary data.

QUANTIFICATION AND STATISTICAL ANALYSIS

Image analysis—Confocal images were analyzed using ImageJ (FIJI)[70]. GFP$^+$ V1 neurons were marked and counted using the ImageJ Cell Counter. Segment boundaries were marked manually using the transmitted light image. For axon tracing, stitched projection images were made with the Pairwise stitching[71] ImageJ plugin. The overlap was dictated by selecting ROIs on both images and the fused image smoothened with linear blending. Images were registered using the fluorescent channel. Number of segments traversed by V1 axons were counted manually from the stitched images.

Analysis of electrophysiology data: Electrophysiology data were imported into Igor Pro 6.37 (Wavemetrics) using NeuroMatic[72]. Spikes and IPSCs were analyzed using custom code in Igor and MATLAB. Charge transfer for the evoked response was calculated by integrating the current in a 50 ms window from the onset of the optical stimulus (Evoked) and subtracting this from Control 1, a similar integral over a 50 ms window before the optical stimulus (Fig. S3). This was done to account for spontaneous activity. To calculate background noise values, a similar integral for a different 50 ms window at the end of the recording (Control 2) was subtracted from Control 1 (Fig. S3). Both the charge transfer of the evoked response and background noise were summed across the 16 squares for each segment.

$$Charge\,transfer(Segment\ i, square\ j) = Evoked(i, j) - Control\ 1(i, j)$$
$$Noise(Segment\ i, square\ j) = Control\ 2(i, j) - Control\ 1(i, j)$$
$$Total\ evoked\ charge\ transfer\ (Seg\ i) = \sum_{j=1}^{16} Charge\ transfer(i, j)$$
$$Total\ noise\ (Seg\ i) = \sum_{j=1}^{16} Noise\ (i, j)$$

For statistical comparisons, *Total evoked charge transfer (Seg i)* was compared to *Total noise (Seg i)* for each target population using the Wilcoxon Sign Rank Test ($p<0.01$).

Peak amplitudes of IPSCs were calculated from the first IPSC only to avoid effects from synaptic depression/facilitation. Conductances were calculated from peak amplitude / driving force (75 mV). Input resistances was measured by an average of small hyperpolarizing pulses.

Statistics—Statistical tests were performed using MATLAB (R2020b, MathWorks). Due to the non-normal distribution of physiological results, including spiking and IPSC charge transfer, we chose to use nonparametric statistics and tests for representations and comparisons. Details of statistical tests, p values used, and Ns are described in the corresponding sections in the Results.

Supplementary Material

Refer to Web version on PubMed Central for supplementary material.

Acknowledgments:

We would like to thank Dr. David McLean and Dr. Sandeep Kishore for kindly providing us with the *mnx:pTagRFP* construct and Dr. Rich Roberts for helping create the *Tg(mnx:pTagRFP)stl603* fish line. All microscopy experiments were performed in part through the use of Washington University Center for Cellular Imaging (WUCCI) supported by Washington University School of Medicine, The Children's Discovery Institute of Washington University and St. Louis Children's Hospital (CDI-CORE-2015-505 and CDI-CORE-2019-813) and the Foundation for Barnes-Jewish Hospital (3770 and 4642). This research was funded by the Pew Scholar Award (M.W.B), R01 DC016413 (M.W.B), a McKnight Scholar Award (M.W.B.), and the McDonnell Center for Cellular and Molecular Neurobiology Postdoctoral Fellowship 2021 (M.S.).

References:

1. Isaacson JS, and Scanziani M (2011). How inhibition shapes cortical activity. Neuron 72, 231–243. [PubMed: 22017986]
2. Goulding M (2009). Circuits controlling vertebrate locomotion: moving in a new direction. Nature reviews. Neuroscience 10, 507–518. [PubMed: 19543221]
3. Talpalar AE, Bouvier J, Borgius L, Fortin G, Pierani A, and Kiehn O (2013). Dual-mode operation of neuronal networks involved in left-right alternation. Nature 500, 85–88. [PubMed: 23812590]
4. Kimura Y, and Higashijima S ichi (2019). Regulation of locomotor speed and selection of active sets of neurons by V1 neurons. Nature Communications 10.
5. Crone SA, Quinlan KA, Zagoraiou L, Droho S, Restrepo CE, Lundfald L, Endo T, Setlak J, Jessell TM, Kiehn O, et al. (2008). Genetic Ablation of V2a Ipsilateral Interneurons Disrupts Left-Right Locomotor Coordination in Mammalian Spinal Cord. Neuron 60, 70–83. [PubMed: 18940589]
6. Gosgnach S, Lanuza GM, Butt SJB, Saueressig H, Zhang Y, Velasquez T, Riethmacher D, Callaway EM, Kiehn O, and Goulding M (2006). V1 spinal neurons regulate the speed of vertebrate locomotor outputs. Nature 440, 215–219. [PubMed: 16525473]
7. Bagnall MW, and Mclean DL (2014). Modular Organization of Axial Microcircuits in Zebrafish. Science 343, 197–200. [PubMed: 24408436]
8. Menelaou E, and McLean DL (2019). Hierarchical control of locomotion by distinct types of spinal V2a interneurons in zebrafish. Nature Communications 10.
9. Knafo S, and Wyart C (2018). Active mechanosensory feedback during locomotion in the zebrafish spinal cord. Current Opinion in Neurobiology 52, 48–53. [PubMed: 29704750]
10. Danner SM, Zhang H, Shevtsova NA, Borowska-Fielding J, Deska-Gauthier D, Rybak IA, and Zhang Y (2019). Spinal V3 Interneurons and Left–Right Coordination in Mammalian Locomotion. Frontiers in Cellular Neuroscience 13.
11. Ruder L, Takeoka A, and Arber S (2016). Long-Distance Descending Spinal Neurons Ensure Quadrupedal Locomotor Stability. Neuron 92, 1063–1078. [PubMed: 27866798]
12. Dale N (2003). Coordinated Motor Activity in Simulated Spinal Networks Emerges from Simple Biologically Plausible Rules of Connectivity. Journal of Computational Neuroscience 14, 55–70. [PubMed: 12435924]
13. Kishore S, Cadoff EB, Agha MA, and Mclean DL (2020). Orderly compartmental mapping of premotor inhibition in the developing zebrafish spinal cord. Science 370, 431–436. [PubMed: 33093104]
14. Jan Ijspeert A, Crespi A, Ryczko D, and Cabelguen J-M (2007). From Swimming to Walking with a Salamander Robot Driven by a Spinal Cord Model. Science 315, 1416–1420. [PubMed: 17347441]
15. Müller UK, and van Leeuwen JL (2004). Swimming of larval zebrafish: Ontogeny of body waves and implications for locomotory development. Journal of Experimental Biology 207, 853–868.
16. Wiggin TD, Peck JH, and Masino MA (2014). Coordination of fictive motor activity in the larval zebrafish is generated by non-segmental mechanisms. PLoS ONE 9.
17. Li H, Yang C, Yusoff NM, Yahaya BH, and Lin J (2017). Direction of commissural axon projections in different regions of the spinal cord during chicken embryonic development. Neuroscience 358, 269–276. [PubMed: 28687312]
18. Yoshida M, Roberts A, and Soffe SR (1998). Axon Projections of Reciprocal Inhibitory Interneurons in the Spinal Cord of Young Xenopus Tadpoles and Implications for the Pattern of Inhibition During Swimming and Struggling. J. Comp. Neurol 400, 504–518. [PubMed: 9786411]
19. Higashijima SI, Masino MA, Mandel G, and Fetcho JR (2004). Engrailed-1 expression marks a primitive class of inhibitory spinal interneuron. Journal of Neuroscience 24, 5827–5839. [PubMed: 15215305]
20. Menelaou E, Vandunk C, and McLean DL (2014). Differences in the morphology of spinal V2a neurons reflect their recruitment order during swimming in larval Zebrafish. Journal of Comparative Neurology 522, 1232–1248.

21. Moran-Rivard L, Kagawa T, Saueressig H, Gross MK, Burrill J, and Goulding M (2001). Evx1 Is a Postmitotic Determinant of V0 Interneuron Identity in the Spinal Cord. Neuron 29, 385–399. [PubMed: 11239430]
22. Saueressig H, Burrill J, and Goulding M (1999). Pathfinding by EN1 spinal interneurons. Development 126, 4201–4212. [PubMed: 10477289]
23. Li WC, Higashijima SI, Parry DM, Roberts A, and Soffe SR (2004). Primitive roles for inhibitory interneurons in developing frog spinal cord. Journal of Neuroscience 24, 5840–5848. [PubMed: 15215306]
24. Falgairolle M, and O'Donovan MJ (2019). V1 interneurons regulate the pattern and frequency of locomotor-like activity in the neonatal mouse spinal cord. PLoS Biology 17.
25. Britz O, Zhang J, Grossmann KS, Dyck J, Kim JC, Dymecki S, Gosgnach S, and Goulding M (2015). A genetically defined asymmetry underlies the inhibitory control of flexor-extensor locomotor movements. eLife 4.
26. Zhang J, Lanuza GM, Britz O, Wang Z, Siembab VC, Zhang Y, Velasquez T, Alvarez FJ, Frank E, and Goulding M (2014). V1 and V2b interneurons secure the alternating flexor-extensor motor activity mice require for limbed locomotion. Neuron 82, 138–150. [PubMed: 24698273]
27. Alvarez FJ, Jonas PC, Sapir T, Hartley R, Berrocal MC, Geiman EJ, Todd AJ, and Goulding M (2005). Postnatal phenotype and localization of spinal cord V1 derived interneurons. Journal of Comparative Neurology 493, 177–192.
28. Saywell SA, Ford TW, and Kirkwood PA (2013). Axonal projections of renshaw cells in the thoracic spinal cord. Physiological Reports 1, 1–12.
29. Fyffe REW (1991). Spatial Distribution of Recurrent Inhibitory Synapses on Spinal Motoneurons in the Cat. Journal of Neurophysiology 65, 1134–1149. [PubMed: 1869909]
30. Kleinlogel S, Feldbauer K, Dempski RE, Fotis H, Wood PG, Bamann C, and Bamberg E (2011). Ultra light-sensitive and fast neuronal activation with the Ca 2+-permeable channelrhodopsin CatCh. Nature Neuroscience 14, 513–518. [PubMed: 21399632]
31. McLean DL, Fan J, Higashijima SI, Hale ME, and Fetcho JR (2007). A topographic map of recruitment in spinal cord. Nature 446, 71–75. [PubMed: 17330042]
32. Menelaou E, and McLean DL (2012). A gradient in endogenous rhythmicity and oscillatory drive matches recruitment order in an axial motor pool. The Journal of neuroscience 32, 10925–10939. [PubMed: 22875927]
33. Ampatzis K, Song J, Ausborn J, and ElManira A (2014). Separate Microcircuit Modules of Distinct V2a Interneurons and Motoneurons Control the Speed of Locomotion. Neuron 83, 934–943. [PubMed: 25123308]
34. Jankowska E, and Smith DO (1973). Antidromic Activation of Renshaw Cells and their Axonal Projections. Acta Physiologica Scandinavica 88.
35. Wu M-Y, Carbó-Tano M, Mirat O, Lejeune F-X, Roussel J, Quan F, Fidelin K, and Wyart CSpinal sensory neurons project onto hindbrain to stabilize posture and enhance locomotor speed. Biorxiv.
36. Kimura Y, Satou C, and Higashijima SI (2008). V2a and V2b neurons are generated by the final divisions of pair-producing progenitors in the zebrafish spinal cord. Development 135, 3001–3005. [PubMed: 18684740]
37. Song J, Dahlberg E, and el Manira A (2018). V2a interneuron diversity tailors spinal circuit organization to control the vigor of locomotor movements. Nature Communications 9.
38. Kimura Y, Satou C, Fujioka S, Shoji W, Umeda K, Ishizuka T, Yawo H, and Higashijima SI (2013). Hindbrain V2a neurons in the excitation of spinal locomotor circuits during zebrafish swimming. Current Biology 23, 843–849. [PubMed: 23623549]
39. Cregg JM, Leiras R, Montalant A, Wanken P, Wickersham IR, and Kiehn O (2020). Brainstem neurons that command mammalian locomotor asymmetries. Nature Neuroscience 23, 730–740. [PubMed: 32393896]
40. Eklöf Ljunggren E, Haupt S, Ausborn J, Ampatzis K, and el Manira A (2014). Optogenetic activation of excitatory premotor interneurons is sufficient to generate coordinated locomotor activity in larval zebrafish. Journal of Neuroscience 34, 134–139. [PubMed: 24381274]
41. Callahan RA, Roberts R, Sengupta M, Kimura Y, Higashijima S-I, and Bagnall MW (2019). Spinal V2b neurons reveal a role for ipsilateral inhibition in speed control. eLife 8.

42. Kimura Y, Okamura Y, and Higashijima SI (2006). alx, a zebrafish homolog of Chx10, marks ipsilateral descending excitatory interneurons that participate in the regulation of spinal locomotor circuits. Journal of Neuroscience 26, 5684–5697. [PubMed: 16723525]
43. Knogler LD, and Drapeau P (2014). Sensory gating of an embryonic zebrafish interneuron during spontaneous motor behaviors. Frontiers in Neural Circuits 8.
44. Higashijima SI, Schaefer M, and Fetcho JR (2004). Neurotransmitter properties of spinal interneurons in embryonic and larval zebrafish. Journal of Comparative Neurology 480, 19–37.
45. Wells S, Nornes S, and Lardelli M (2011). Transgenic zebrafish recapitulating tbx16 gene early developmental expression. PLoS ONE 6.
46. del Barrio MG, Bourane S, Grossmann K, Schüle R, Britsch S, O'Leary DDM, and Goulding M (2013). A transcription factor code defines nine sensory interneuron subtypes in the mechanosensory area of the spinal cord. PLoS ONE 8.
47. Gatto G, Bourane S, Ren X, di Costanzo S, Fenton PK, Halder P, Seal RP, and Goulding MD (2021). A Functional Topographic Map for Spinal Sensorimotor Reflexes. Neuron 109, 1–14. [PubMed: 33412092]
48. Hale ME, Ritter DA, and Fetcho JR (2001). A Confocal Study of Spinal Interneurons in Living Larval Zebrafish. J. Comp. Neurol 437, 1–16. [PubMed: 11477593]
49. Wells S, Conran JG, Tamme R, Gaudin A, Webb J, and Lardelli M (2010). Cryptic organisation within an apparently irregular rostrocaudal distribution of interneurons in the embryonic zebrafish spinal cord. Experimental Cell Research 316, 3292–3303. [PubMed: 20599944]
50. Todd AJ, and Mckenzie J (1989). GABA-IMMUNOREACTIVE NEURONS IN THE DORSAL HORN OF THE RAT SPINAL CORD.
51. Satou C, Kimura Y, and Higashijima S. ichi (2012). Generation of multiple classes of V0 neurons in Zebrafish spinal cord: Progenitor heterogeneity and temporal control of neuronal diversity. Journal of Neuroscience 32, 1771–1783. [PubMed: 22302816]
52. Satou C, Sugioka T, Uemura Y, Shimazaki T, Zmarz P, Kimura Y, and Higashijima S. ichi (2020). Functional Diversity of Glycinergic Commissural Inhibitory Neurons in Larval Zebrafish. Cell Reports 30, 3036–3050.e4. [PubMed: 32130905]
53. Griener A, Zhang W, Kao H, Wagner C, and Gosgnach S (2015). Probing diversity within subpopulations of locomotor-related V0 interneurons. Developmental Neurobiology 75, 1189–1203. [PubMed: 25649879]
54. Juárez-Morales JL, Schulte CJ, Pezoa SA, Vallejo GK, Hilinski WC, England SJ, de Jager S, and Lewis KE (2016). Evx1 and Evx2 specify excitatory neurotransmitter fates and suppress inhibitory fates through a Pax2-independent mechanism. Neural Development 11, 1–20. [PubMed: 26782621]
55. Satou C, Sugioka T, Uemura Y, Shimazaki T, Zmarz P, Kimura Y, and Higashijima S. ichi (2020). Functional Diversity of Glycinergic Commissural Inhibitory Neurons in Larval Zebrafish. Cell Reports 30, 3036–3050.e4. [PubMed: 32130905]
56. Roussel Y, Gaudreau S, Sengupta M, and Bui T. v (2021). Modelling spinal locomotor circuits for movements in developing zebrafish. Biorxiv, undefined.
57. Izhikevich EM (2003). Simple model of spiking neurons. IEEE Transactions on Neural Networks 14, 1569–1572. [PubMed: 18244602]
58. Bikoff JB, Gabitto MI, Rivard AF, Drobac E, MacHado TA, Miri A, Brenner-Morton S, Famojure E, Diaz C, Alvarez FJ, et al. (2016). Spinal Inhibitory Interneuron Diversity Delineates Variant Motor Microcircuits. Cell 165, 207–219. [PubMed: 26949184]
59. Alvarez FJ, Benito-Gonzalez A, and Siembab VC (2013). Principles of interneuron development learned from Renshaw cells and the motoneuron recurrent inhibitory circuit. Annals of the New York Academy of Sciences 1279, 22–31. [PubMed: 23530999]
60. Siembab VC, Smith CA, Zagoraiou L, Berrocal MC, Mentis GZ, and Alvarez FJ (2010). Target selection of proprioceptive and motor axon synapses on neonatal V1-derived Ia inhibitory interneurons and Renshaw cells. Journal of Comparative Neurology 518, 4675–4701.
61. Bello-Rojas S, Istrate AE, Kishore S, and McLean DL (2019). Central and peripheral innervation patterns of defined axial motor units in larval zebrafish. Journal of Comparative Neurology 527, 2557–2572.

62. Tunstall MJ, and Roberts A (1994). A longitudinal gradient of synaptic drive in the spinal cord of Xenopus embryos and its role in co-ordination of swimming. Journal of Physiology 474, 393–405.

63. Hubbard JM, Böhm UL, Prendergast A, Tseng PEB, Newman M, Stokes C, and Wyart C (2016). Intraspinal Sensory Neurons Provide Powerful Inhibition to Motor Circuits Ensuring Postural Control during Locomotion. Current Biology 26, 2841–2853. [PubMed: 27720623]

64. Böhm UL, Prendergast A, Djenoune L, Figueiredo SN, Gomez J, Stokes C, Kaiser S, Suster M, Kawakami K, Charpentier M, et al. (2016). CSF-contacting neurons regulate locomotion by relaying mechanical stimuli to spinal circuits. Nature Communications 7, 1–8.

65. O'leary DDM, and Terashima T (1988). Cortical Axons Branch to Multiple Subcortical Targets by Interstitial Axon Budding: Implications for Target Recognition and 'Waiting Periods". Neuron 1, 901–910. [PubMed: 3272157]

66. Petreanu L, Huber D, Sobczyk A, and Svoboda K (2007). Channelrhodopsin-2-assisted circuit mapping of long-range callosal projections. Nature Neuroscience 10, 663–668. [PubMed: 17435752]

67. Kimura Y, Hisano Y, Kawahara A, and Higashijima SI (2014). Efficient generation of knock-in transgenic zebrafish carrying reporter/driver genes by CRISPR/Cas9-mediated genome engineering. Scientific Reports 4, 1–7.

68. Arrenberg AB, del Bene F, and Baier H (2009). Optical control of zebrafish behavior with halorhodopsin. Proceedings of the National Academy of Sciences 106.

69. McDearmid JR, and Drapeau P (2006). Rhythmic motor activity evoked by NMDA in the spinal zebrafish larva. Journal of Neurophysiology 95, 401–417. [PubMed: 16207779]

70. Schindelin J, Arganda-Carreras I, Frise E, Kaynig V, Longair M, Pietzsch T, Preibisch S, Rueden C, Saalfeld S, Schmid B, et al. (2012). Fiji: An open-source platform for biological-image analysis. Nature Methods 9, 676–682. [PubMed: 22743772]

71. Preibisch S, Saalfeld S, and Tomancak P (2009). Globally optimal stitching of tiled 3D microscopic image acquisitions. Bioinformatics 25, 1463–1465. [PubMed: 19346324]

72. Rothman JS, and Silver RA (2018). Neuromatic: An integrated open-source software toolkit for acquisition, analysis and simulation of electrophysiological data. Frontiers in Neuroinformatics 12.

Highlights

Mapped connectivity from spinal V1 neurons to targets along the longitudinal axis.

Despite long axons, V1s inhibit motor and premotor neurons only locally.

Sensory CoPA neurons receive both local and long range V1 inhibition.

Local V1 inhibition to motor targets is required for reliable locomotion.

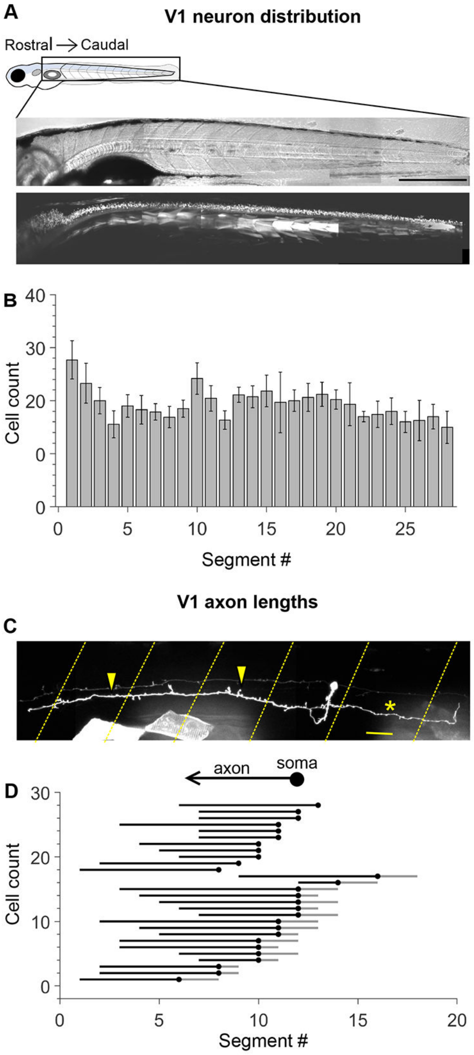

Figure 1: Engrailed^{+} V1 neurons project long, primarily ascending axons.

A. Transmitted light image (top) and confocal image (bottom) of a 5 dpf *Tg (eng1b:Gal4,UAS:GFP)* larva. In this and subsequent Figures, rostral is to the left and dorsal to the top. Some non-specific expression of GFP is present in muscle fibers as well. Scale bar: 0.5 mm B. Bar plot showing mean cell count of V1 neurons per segment along the rostro-caudal axis. n = 15 larvae from 4 clutches. Error bars represent SEM. C. Representative example of a sparsely labelled V1 neuron in a mid-body segment. Segment borders are shown in yellow dashed lines. Arrowheads mark the ascending axon, and the asterisk marks the descending axon. Scale bar: 20 μm. D. Ball and stick plots representing the soma (ball) and ascending and descending axon lengths of V1 neurons (sticks) relative to body segments. N = 28 neurons from 18 larvae. See also Figure S1.

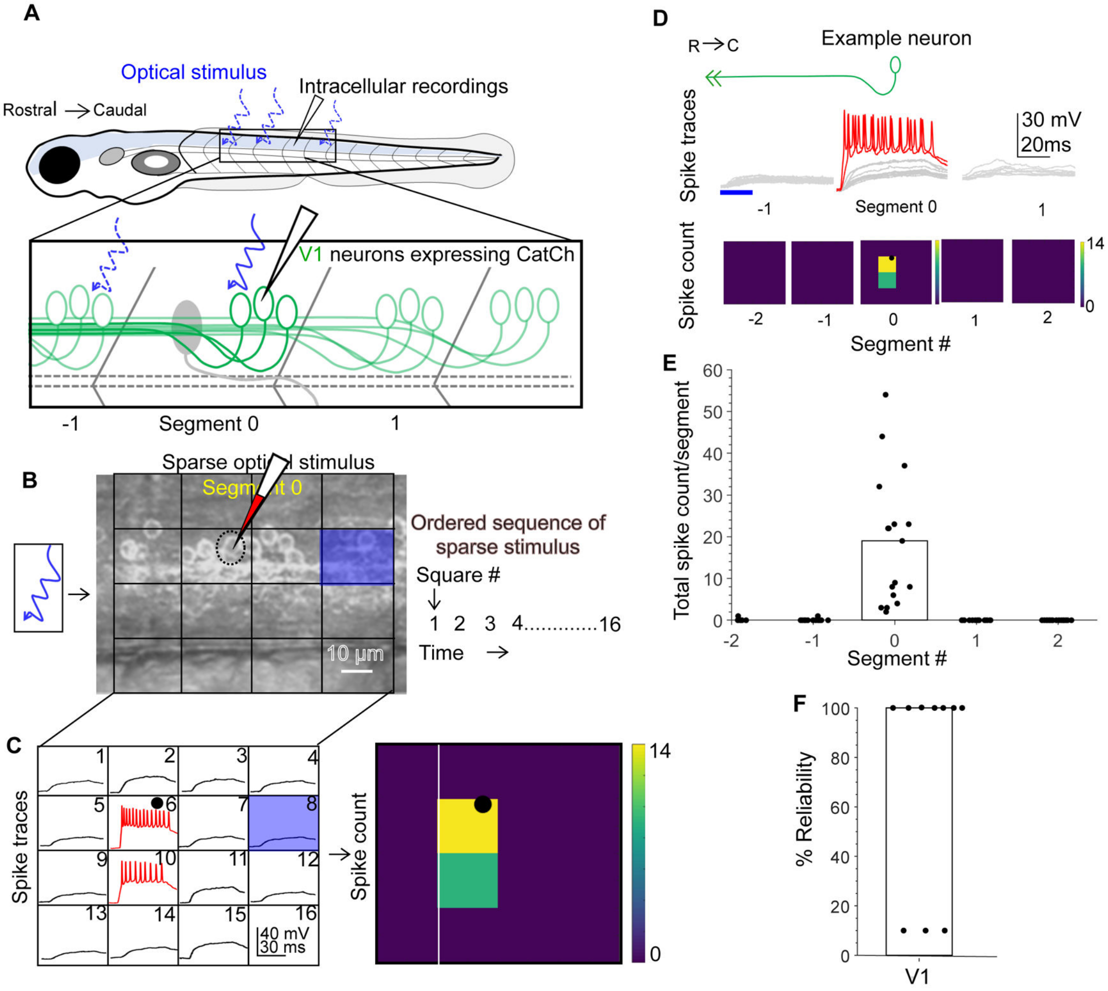

Figure 2: Calibration of V1 spiking evoked by optical stimulus.

A. Schematic of the experimental set-up showing targeted intracellular recording and optical stimulation in *Tg(eng1b:Gal4,UAS:CatCh)* animals. B. Schematic of the patterned optical stimulus. A 4x4 grid was overlaid on approximately one segment and each square in the grid (blue square) was optically stimulated in an ordered sequence (right). Position of the recorded cell is shown as a dotted black circle. C. Illustration of the analysis. Intracellular recordings elicited from optical stimulation in each grid square (left). Spiking is denoted in red. Same data shown as a heat map and superimposed on the optical stimulus grid (right). Position of the recorded cell is indicated with a black circle. D. V1 responses evoked by optical stimuli in segments rostral or caudal to the recorded neuron. Representative traces of activity (top) and spike count (bottom) of the same V1 neuron while the optical stimulation was moved along the rostro-caudal axis. Red traces indicate spiking. E. Quantification of spiking in V1 neurons as the optical stimulus is presented along the rostro-caudal axis. N = 17 neurons. Bar indicates median value. F. Reliability of spiking in these neurons with multiple trials of the same optical stimulus. N=10 neurons. Bar indicates median value. See also Figure S2.

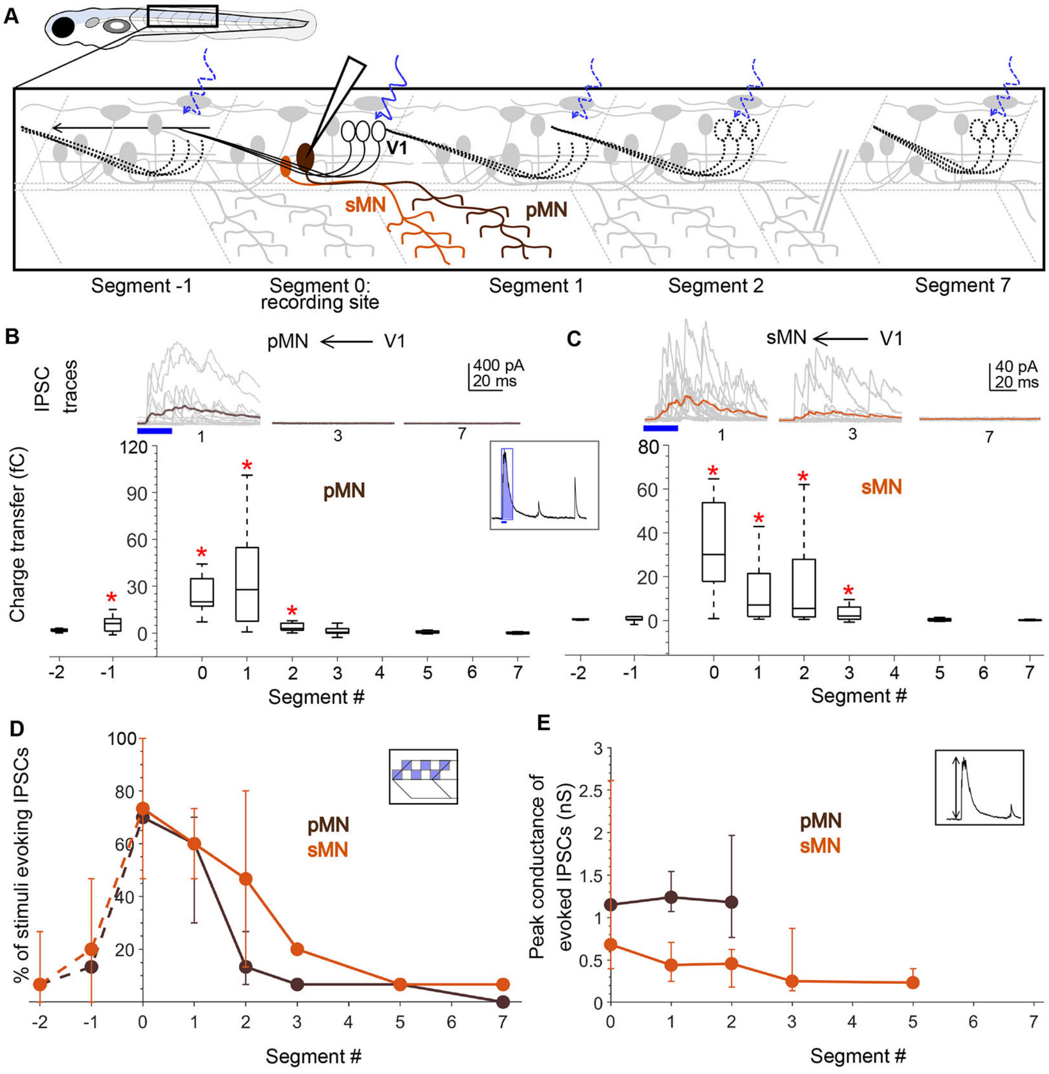

Figure 3: Motor neurons receive input only from local V1 neurons.

A. Schematic of the experimental design showing intracellular recordings from primary (brown) and secondary (orange) motor neurons paired with optical stimulation of V1 neurons (black) along the rostro-caudal axis. B. Top: Representative overlay of 15 traces of IPSCs recorded in a primary motor neuron (pMN) during illumination of segments 1, 3, and 7 caudal to the recorded neuron soma. Colored trace represents mean. Duration of the optical stimulus is shown as a blue bar. Bottom: Box plots showing total charge transfer per segment (inset, illustration) recorded in primary motor neurons. In this and subsequent Figures, the box shows the median, 25th, and 75th percentile values; whiskers show +/−2.7σ. Red asterisks mark segments that were significantly different from noise ($p < 0.01$). N = 8-26 neurons for each data point. C. Same as in B for secondary motor neurons (sMNs). N = 10-11 neurons for each data point. D, E. Comparison of the percent of squares in the optical stimulus grid that evoked IPSCs (D) and the peak conductance of IPSCs (E) in primary (brown) and secondary (orange) motor neurons. Here and in subsequent Figures, circles represent median values and error bars indicate the 25th and 75th percentiles. N= 8-26 pMNs and 11 sMNs. See also Figure S3.

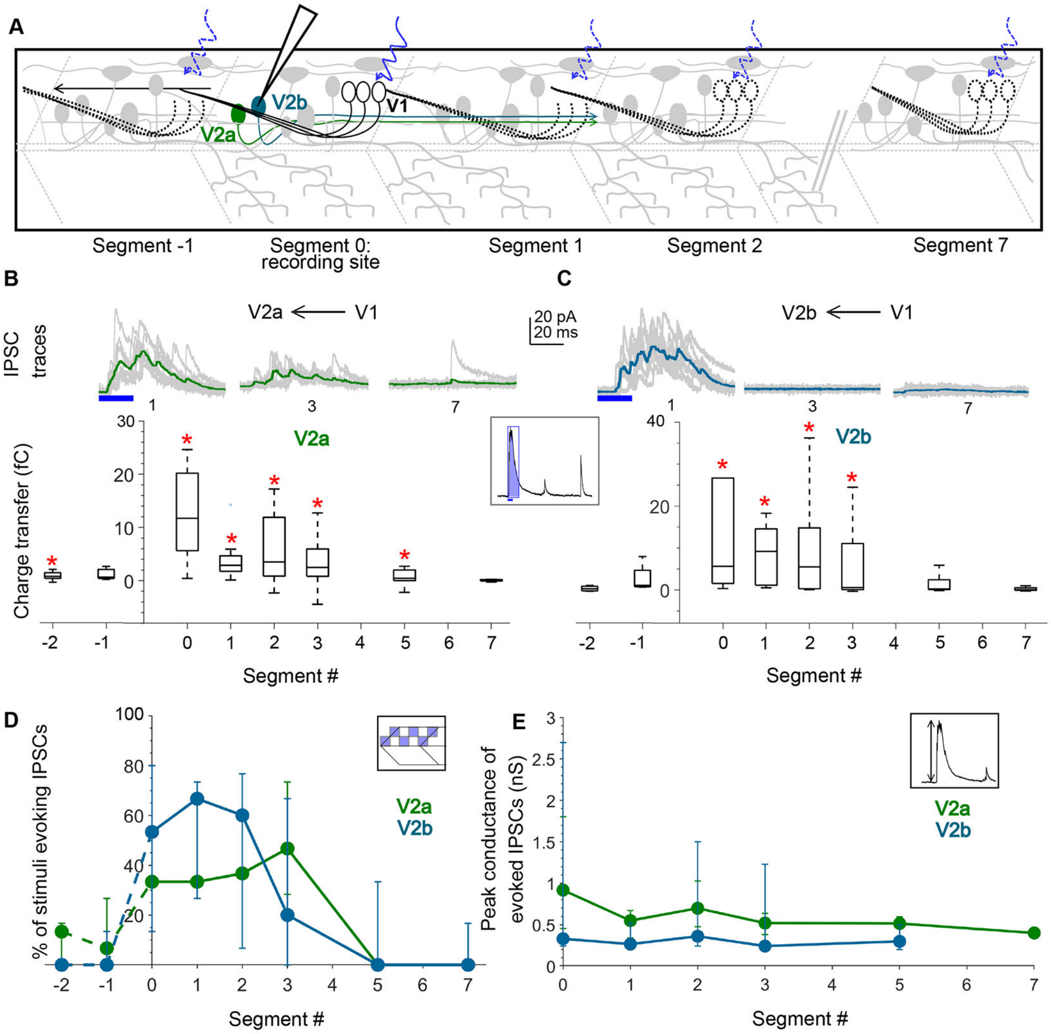

Figure 4: V1 neurons inhibit V2a and V2b neurons locally.

A. Schematic of the experimental design showing intracellular recordings from V2a (green) and V2b (cyan) neurons paired with optical stimulation of V1 neurons (black) along the rostro-caudal axis. B. Top: Representative overlay of 15 traces of IPSCs recorded in V2a neurons during illumination of segments 1, 3, and 7 caudal to the recorded neuron position. Colored trace represents mean. Duration of the optical stimulus is shown as a blue bar. Bottom: Box plots showing the total charge transfer per segment recorded in V2a neurons. Red asterisks mark segments that were significantly different from noise ($p < 0.01$). N = 8-14 neurons for each data point. C. Same as in B for V2b neurons. N = 5-9 neurons. D, E. Comparison of the number of squares in the optical stimuli grid that evoked IPSCs (D) and the peak conductance of IPSCs (E) in V2a (green) and V2b (cyan) neurons. N= 8-14 V2as, 5-9 V2bs. See also Figure S4.

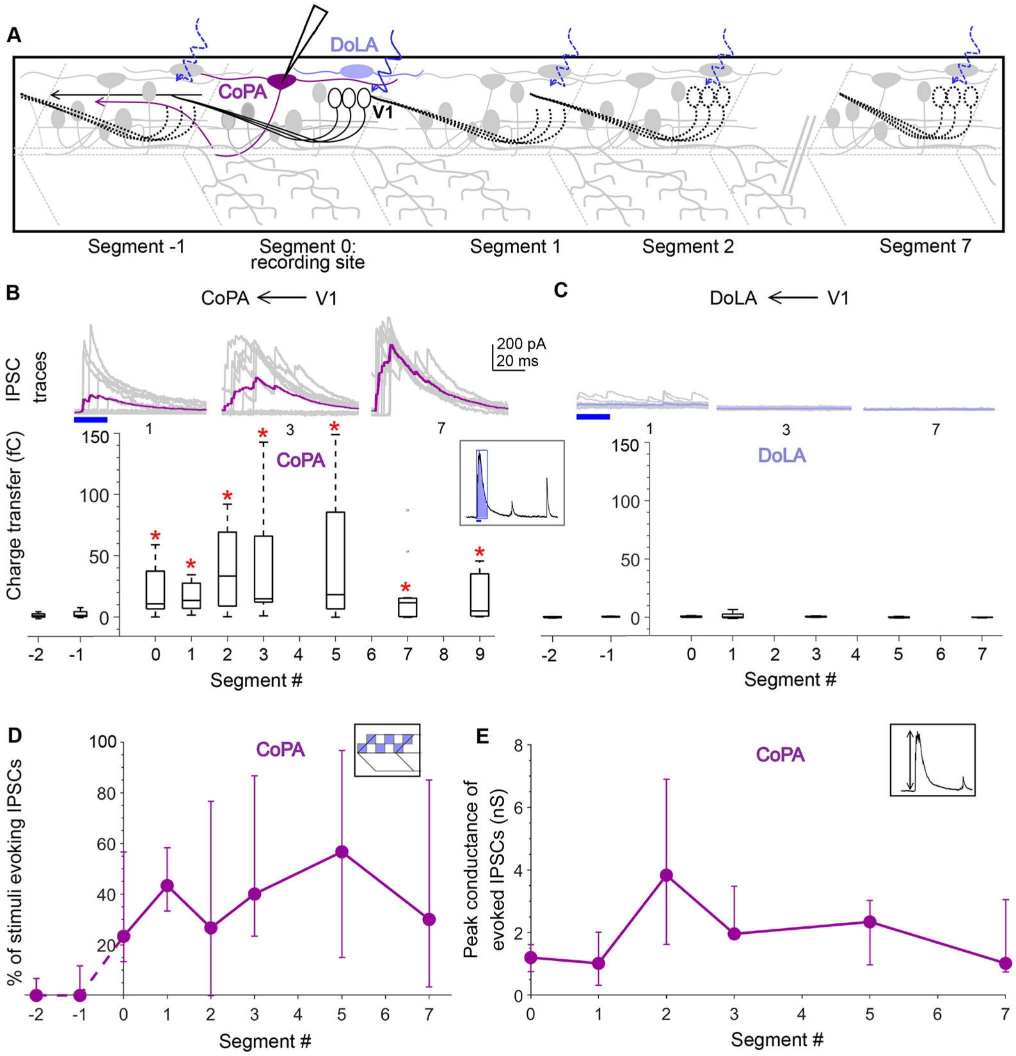

Figure 5: Dorsal horn CoPA neurons receive both local and long-range inputs from V1 neurons.
A. Schematic of the experimental design showing intracellular recordings from CoPA (magenta) and DoLA (violet) neurons paired with optical stimulation of V1 neurons (black) along the rostro-caudal axis. B. Top: Representative overlay of 15 traces of IPSCs recorded in CoPA neurons during illumination of segments 1, 3, and 7 caudal to the recorded neuron position. Colored trace represents mean. Duration of the optical stimulus is shown as a blue bar. Bottom: Box plots showing the total charge transfer per segment recorded in CoPA neurons. Red asterisks mark segments that were significantly different from noise ($p < 0.01$). N = 7 to 12 neurons for each data point. C. Same as in B for DoLA neurons. N = 4-5 neurons for each point. D, E. Comparison of the number of squares in the optical stimuli grid that evoked IPSCs (D) and the peak conductance of IPSCs (E) in CoPA neurons. N = 7-12 neurons. See also Figure S5.

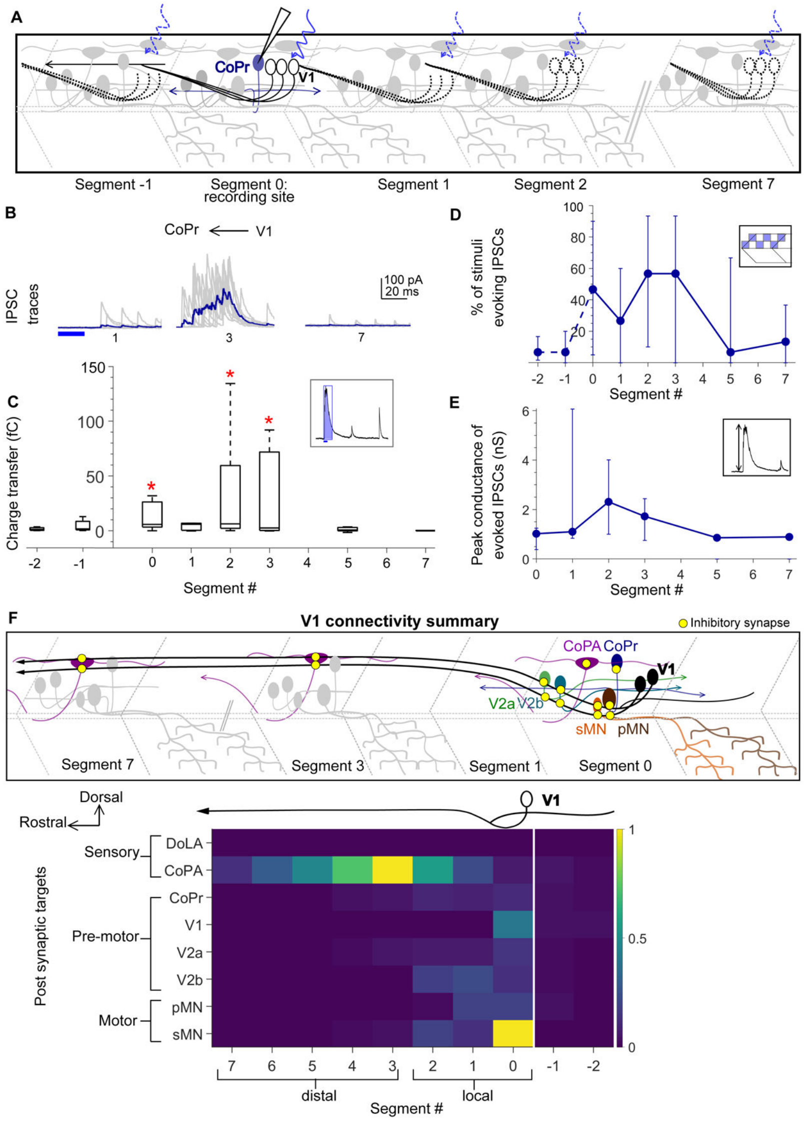

Figure 6: Local V1 synapses onto CoPr neurons and normalized connectivity map.

A. Schematic of the experimental design showing intracellular recording from CoPr neurons (blue) paired with optical stimulation of V1 neurons (black) along the rostro-caudal axis. B, C. Representative traces of IPSCs (B) and the total charge transfer (C) recorded in CoPr neurons with optical stimulation of V1 neurons along different segments in the rostro-caudal axis. Colored traces in B indicate mean. D, E. Comparison of the number of squares in the optical stimuli grid that evoked IPSCs (D) and the conductance of IPSCs (E) in CoPr neurons. N = 5 to 7 neurons for each point. F. Summary of V1 connectivity to different post-synaptic targets. Top: Schematic of the inferred connectivity of V1 neurons (black) to different targets locally and distally. Yellow dots symbolize inhibitory synapses. Bottom: Heat map showing normalized charge transfer for the different post-synaptic targets along the rostro-caudal axis. The charge transfer per segment for each recorded neuronal target was normalized to its measured intrinsic neuronal conductance (inverse of R_{in}). Median values of normalized charge transfer for each target cell population are plotted. Values for

Segment 4 and Segment 6 were interpolated as averages of the two neighboring segments. The resulting values are plotted on the same color scale for all target populations. See also Figure S6.

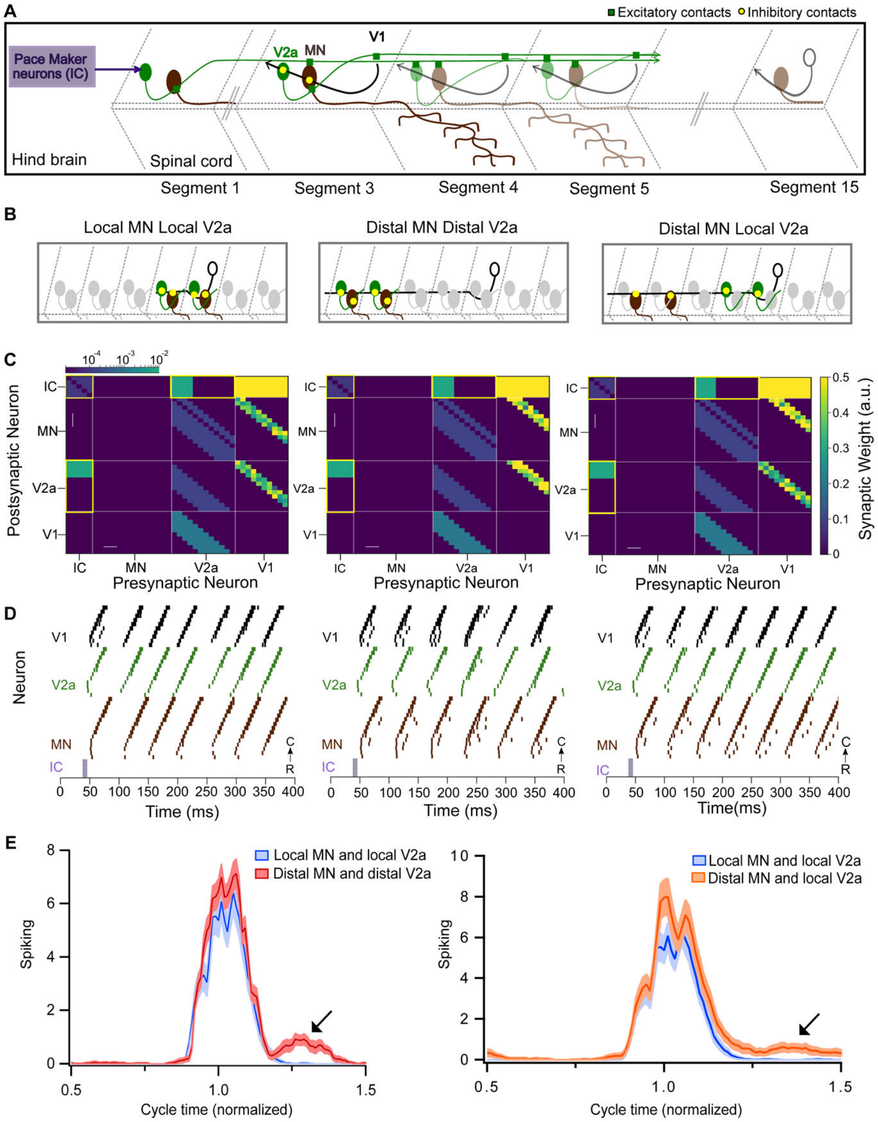

Figure 7: Modeling spinal circuitry with local and distal V1 inhibition.

A. Schematic of the computational model showing a reduced V1 (black), V2a (green), and motor neuron (MN, brown) network driven by rostrally located pacemaker neurons (purple box). B. Schematic of 3 different network structures simulated with the network model. Left: Local MN and local V2a connectivity from V1s. V1s synapse onto V2as and MNs located within 1 to 3 segments. Middle: Distal MN and distal V2a connectivity from V1s. V1s synapse onto V2as and MNs located 4 to 6 segments away. Right: Distal MNs and local V2a connectivity from V1s. V1s synapse onto MNs located 4 to 6 segments away and V2as located within 1 to 3 segments. C. Heatmap showing connectivity weights for neurons across 3 different network models. Connections highlighted in yellow are gap junctional and follow a logarithmic scale. Asterisks indicate altered connections. D. Raster plots of spike times from 1 representative simulation of each network. E. Spiking of MNs with respect to a normalized swim cycle. Black arrow points to the extraneous spiking observed for both distal MN / distal V2a connectivity (left) and more weakly in distal MNs / local V2a connectivity (right). See also Figure S7 and tables S1 and S2.

KEY RESOURCES TABLE

REAGENT or RESOURCE	SOURCE	IDENTIFIER
Antibodies		
Bacterial and virus strains		
Biological samples		
Chemicals, peptides, and recombinant proteins		
Low melt agarose	VWR International	Cat # IB70050
α-bungarotoxin	Tocris, FISHER SCIENTIFIC INTL INC	Cat # 21331
NBQX disodium salt	Abcam	Cat # ab120046
APV	Abcam	Cat # ab120003
Strychnine	Sigma	Cat # S0532
TTX	Abcam	Cat # ab120055
Sulforhodamine B	Sigma	Cat # S1402
Alexa fluor 568 hydrazide	Invitrogen	Cat # A10437
Alexa fluor 647 anionic dextran (MW:10000)	Invitrogen	Cat # D22914
Critical commercial assays		
Deposited data		

Experimental models: Cell lines		
Experimental models: Organisms/strains		
Danio rerio (zebrafish), *Tg(eng1b-hs:Gal4)nns40Tg*	[67]	ZDB-ALT-151202-14
Danio rerio (zebrafish), *Tg(UAS:CatCh)stl602*	[41]	ZDB-ALT-201209-12
Danio rerio (zebrafish), *Tg(vsx2:loxP-DsRed-loxP-GFP)nns3Tg*	[42]	ZDB-ALT-061204-4
Danio rerio (zebrafish), *Tg(gata3:lox-Dsred-lox:GFP)nns53Tg*	[41]	ZDB-ALT-190724-4
Danio rerio (zebrafish), *Tg(mnx:pTagRFP)stl603*	This paper	
Oligonucleotides		
Recombinant DNA		
Plasmid, UAS:Dendra	[68]	N/A
BAC, eng1b:GFP	[19]	N/A
Software and algorithms		
ImageJ	[70,71]	https://imagej.nih.gov/ij/
Igor Pro 6.37, Neuromatic	Wavemetrics, Neuromatic [72]	https://www.wavemetrics.com/
MATLAB	Mathworks	https://www.mathworks.com/products/matlab.html
Computational model	This paper	https://github.com/bagnall-lab/V1_connectivity_project
Other		
